

Design and Analysis of New Ultra Compact Decoupled XYZ θ Stage to Achieve Large-scale High Precision Motion

Xigang Chen^a, Yangmin Li^{a,*}, Yanlin Xie^a and Ruobing Wang^a

^aDepartment of Industrial and Systems Engineering, The Hong Kong Polytechnic University, Hong Kong SAR 999077, China

ARTICLE INFO

Keywords:

Ultra compact structure
Two-stage amplifier
Flexure mechanism design
Decoupled XYZ θ Stage
Large-scale high precision motion

ABSTRACT


High precision motion stage is a crucial component in many modern industrial equipment. The performance index of a high precision motion stage includes the volume, the output travel range, the output resolution and the stability. In this paper, a new high precision ultra-compact decoupled XYZ θ motion stage based on flexure hinges is designed and analyzed which can achieve large-scale output displacement. The stage mainly consists of three components including serial-parallel dual-stage amplifier, Z-shape motion steering mechanism and motion decoupled mechanism. Compared with the existing stages, the proposed high precision motion stage has many advantages such as extremely compact structure, large output decoupling motion and XYZ θ four axes output displacement. The function of serial-parallel dual-stage amplifier is to amplify the travel range of nano positioning piezo actuator (PZT) by connecting two parallel bridge type mechanism. The Z-shape mechanism can change the direction of motion transmission to make the stage more compact and form movement in XYZ θ four directions. The decouple mechanism can reduce the implicative movement of different piezo actuators. Then, kinetostatic analysis of this new XYZ θ stage is conducted to analyze the stage. The kinetostatic analysis method can calculate the input and output force-displacement relationships in multi-degree-of-freedom. Finally, the finite-element analysis (FEA) and prototype experiments are implemented to verify the design objectives.

1. Introduction

High precision motion stages have been applied extensively in biomedical engineering, semiconductor manufacturing, scanning probe microscope and aerospace Engineering, etc. In order to realize micron even nanometer resolution, compliant structure is broadly used in high precision motion stages due to its unique characteristics [1, 2, 3, 4, 5]. Traditional mechanical transmission mechanism cannot avoid friction, assembly error, abrasion, and machining error. By contrast, flexure-based mechanism can effectively overcome these shortcomings [6, 7, 8, 9]. Therefore, the high precision motion stage proposed in this paper adopted the flexure hinges as transmission mechanism. On the other side, high resolution is necessary requirement for high precision motion stages. In order to solve this problem, piezoelectric actuators (PZT) are usually adopted in high precision motion stages. The piezoelectric ceramic actuator not only meets the requirements of high driving force and rigidity but also has very ideal repetitive positioning accuracy, which can ensure high resolution [10, 11].

At present, with the development of integrated circuit industry, aerospace, bioengineering and other fields, higher requirements are put forward for the performance of high-precision motion stages, which not only requires the positioning stages to have high displacement, positioning accuracy and sensitivity, good dynamic characteristics and anti-interference ability, but also requires the high precision positioning stages to have more freedom of motion to achieve precise positioning and large working space. For this reason, many scholars have done a lot of research on high precision motion stages. And the research on high precision motion stages based on piezoelectric ceramics and flexure hinge is a research hotspot. According to the classification of motion direction of high precision motion stages, the compliant high precision motion stages based on piezoelectric ceramics can be divided into one-dimensional, two-dimensional, three-dimensional, and multi-dimensional [12, 13, 14, 15, 16]. In the early research, scholars mainly focused on the planar motion stages, that is one-dimensional and two-dimensional stages. In recent years, researchers have designed micro displacement stages with different dimensions. In 2009, Yuen Kuan Yong et al. from the University of Newcastle, Australia, developed a two dimensional piezoelectric positioning stages with sub nanometer

*Corresponding author

 xigang.chen@connect.polyu.hk (X. Chen); yangmin.li@polyu.edu.hk (Y. Li)

ORCID(s):

resolution [17]. The stage used a lever as an amplification mechanism, with a working range of $25 \times 25 \mu\text{m}^2$ and accurate scanning performance up to 400 Hz. Gao, Nanyang University of technology, Singapore, designed a two dimensional XY motion stage [18]. The stage adopted a flexible hinge lever amplification mechanism, with a maximum working stroke of $45 \mu\text{m} \times 40 \mu\text{m}$, a minimum resonance frequency of 525 Hz and a positioning resolution of 20nm and 18nm.

In order to satisfy the demand of multi-dimensional motion, such as the scanning device in an atomic force microscope (AFM). The design of micro/nano motion stages have experienced the development from single degree of freedom, two degrees of freedom to three degrees of freedom and multi degrees of freedom. For example, Culpepper et al. from MIT have designed a three-dimensional high-precision optical fiber aligner [19]. The maximum working space of the mechanism is $100 \mu\text{m} \times 100 \mu\text{m} \times 100 \mu\text{m}$. Basically, these 3-D high precision motion stages consisted of orthogonal structures and parallel mechanisms. But the three orthogonal flexure hinges structures lead to the large size of stages. Otherwise, most of these stages were short of the decoupling mechanisms that caused coupled motions at the end effector. The implicated motion of the stage creates difficulties to the design of controllers.

Compared with the traditional motion stages, the kinematics analysis of the stages is the primary problem of the mechanical analysis in the design process of the nano motion compliant stages, which is the basis of the dynamic analysis and the end effector precision analysis of the machine. At the same time, the establishment of the kinematic model of the mechanism is also the basis of the design of the control system. For a compliant stage, the stroke of end effector is related to the stiffness and natural frequency of the mechanism. Generally, the stiffness of the compliant stages is larger, the range of its stroke of end effector is smaller and the natural frequency of the system is higher. At present, the theoretical modeling for compliant mechanisms commonly used are simple beam analysis, the principle of virtual work, pseudo rigid body model and the compliance matrix method. In literature [20], the multi-stage compliant mechanism was analyzed by the principle of virtual work. For complex series-parallel flexure hinge mechanism, the compliance matrix method is usually used due to its calculation is simple. For instance, Li et al. [21] and Jiang et al. [22] proposed some kinetostatic modeling methods for flexure hinge mechanisms using the compliance matrix method.

In this paper, a novel ultra-compact XYZ θ high precision motion stage with large scale output displacement is proposed. The flexure hinge motion stage used a dual-stage series bridge amplifier to enlarge the output displacement. In order to make the whole motion stage more compact, a z-shape flexure hinge was adopted to change the direction of motion transmission. Then, a kinetostatic modeling method based on compliance matrix method was proposed to analyze the kinematic and static characteristics of the new stage. As a most popular method for analyzing kinetostatics, finite elemental method was used for verifying the effectiveness of modeling. The rest of this paper is organized as follows. In Section 2, the detailed mechanical design procedures are presented. In Section 3, the kinematic and static modeling of the novel XYZ θ stage is conducted using a new kinetostatic modeling method. Then, the modeling results are validated by finite elemental analysis in Section 4. In addition, a prototype of the designed XYZ θ stage is established by 3D printing method and a series of experiments are implemented in Section 5. Finally, the conclusions are presented in Section 6 along with future works indicated.

2. Mechanical Design of Ultra Compact Decoupled XYZ θ Stage

The mechanical design is the most important issue for high precision XYZ θ motion stage. The mechanical structure determines the performance of the XYZ θ stage. In this research, the objectives are to establish a XYZ θ micro motion stage with as compact as possible and large-scale decoupled output displacement. Therefore, a decoupled structure, an output amplified mechanism and a motion transmission changer are designed for this XYZ θ stage.

2.1. The decoupling mechanism

In most of previous micro motion stages, the parasitic motion of end effector is inescapable due to a lack of decoupled mechanism. Fig. 1 shows the structure of the decoupling mechanism with the end effector platform. The decoupling mechanism contains the right-circular flexure hinges as shown in Fig. 2 and it relates to the end effector platform in parallel style to improve the stability and stiffness. The decoupling mechanism can make each driving chain of micro motion stage not interfere with each other.

2.2. The dual-stage amplified mechanism

As mentioned in above, piezoelectric actuators are usually applied in compliant mechanism micro motion stages on account of its large output drive force, high stiffness, and high response frequency. Fig. 3 presents a basic one-stage

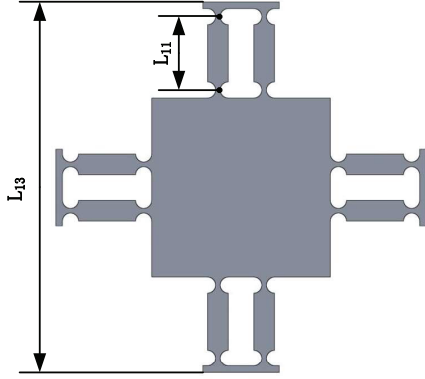


Figure 1: The structure of the decoupling mechanism.

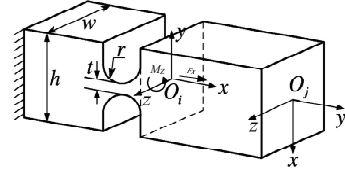


Figure 2: The right-circular flexure hinges.

bridge type amplifier. As shown in Fig. 4, the flexure hinge amplifier adopts two bridge type amplifiers connected in series. This mechanical structure can enlarge the input displacement of PZTs as much as possible. According to the previous study [23], the dual-stage can obviously improve the amplification ratio compared with the one-stage amplifier.

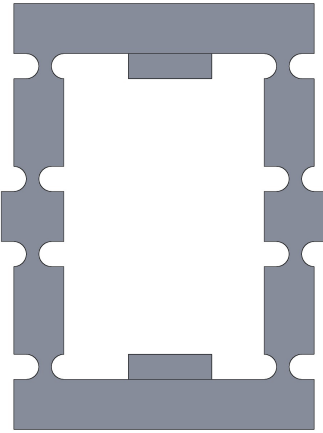


Figure 3: Basic one-stage bridge type amplifier.

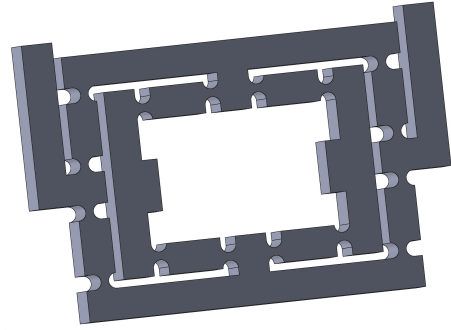


Figure 4: Dual-stage bridge type amplifier.

2.3. Z-shape motion steering mechanism

Fig. 5 presents a Z-shape flexure hinge. The functions of this Z-shape mechanism are to transfer the amplifiers output displacement and decouple the parasitic motion in Z axis. At the same time, The Z-shape flexure hinge will produce the output displacement in X axis when its input displacement is in Y axis. Thus, the Z-shape flexure hinge mechanism can change the transmission direction of dual-stage flexure hinge amplifier.

2.4. A ultra-compact decoupled XYZ θ stage with large scale output displacement

As shown in Fig. 6, the one limb of the XYZ θ stage can produce the output displacement in two directions. Therefore, a new XYZ θ stage can be established by combining four dual-stage bridge type amplifiers with the Z-shape motion steering flexure hinge mechanism. The ultra-compact decoupled XYZ θ stage (UCDS) is different from the traditional XYZ micro motion stage. The traditional micro motion stages [24, 25] usually adopted orthogonal arrangement to realize three axes motion. However, the micro motion stages might be too large if the orthogonal arrangement is used. The structure of the ultra-compact decoupled XYZ θ stage (UCDS) as shown in Fig. 7 can effectively modify the

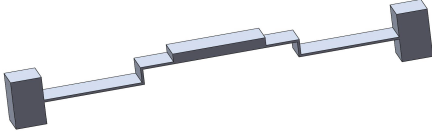


Figure 5: Z-shape motion steering mechanism.

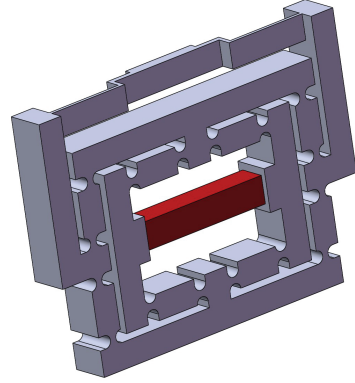


Figure 6: One limb of the $XYZ\theta$ stage.

drawbacks of orthogonal arrangement. In addition, the design of decoupling mechanism can alleviate the influence of parasitic motion to protect the PZTs by avoiding transverse loads.

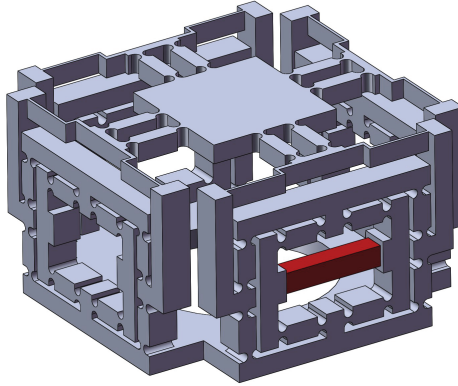


Figure 7: The structure of the ultra-compact decoupled $XYZ\theta$ stage (UCDS).

3. Modeling and analysis

The flexure hinge mechanism is formed with three components: flexure hinge, flexible beam and lumped mass. As shown in Fig. 2, the parameters of the circular flexure hinge are illustrated. The ultra-compact decoupled $XYZ\theta$ stage (UCDS) adopts monolithic circular flexure hinge presented in Fig. 2. According to specifications of the drive and structures, the flexure hinge mainly suffered from a bending torque M_Z and tension-compression along the longitudinal axis F_x . Hence, the flexure hinge can be substituted by a torsion spring and a coil spring in dynamical model. Its equivalent mathematical model is presented in Fig. 8. The stiffness of the springs are K_r and K_t , respectively. As for the relationships of the parameters of circular flexure hinge with the stiffness K_r and K_t , there are some different stiffness/compliance empirical equations proposed for calculating these characteristics of circular flexure hinge [26, 27, 28, 29, 30, 31]. In this paper, the stiffness/compliance equations proposed in literature [26] were adopted as follows:

$$K_r = \frac{Ewt^3(2r+t)(4r+t)^3}{24r \left[\begin{array}{l} t(4r+t)(6r^2+4rt+t^2) \\ +6r(2r+t)^2\sqrt{t(4r+t)} \arctan\left(\sqrt{1+\frac{4r}{t}}\right) \end{array} \right]} \quad (1)$$

$$K_t = \frac{Ew\sqrt{t(4r+t)}}{2(2r+t)(\arctan \sqrt{1+\frac{4r}{t}} - \frac{\pi}{2})} \quad (2)$$

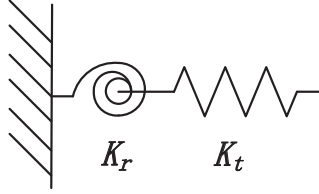


Figure 8: Equivalent mathematical dynamic model of the flexure hinge.

3.1. Kinematics and statics analysis based on simplified model

As presented in above sections, the proposed XYZ θ stage contains four limbs. Every limb has same structures and parameters and can achieve two degree-of-freedom motion. Hence, the kinematics and statics modeling for the single limb are the basis of the whole XYZ θ stage's modeling.

As is well-known, the calculations of the input stiffness for each actuator and the input/output amplification ratio are the main issues for kinematics and statics analysis of compliant micro motion stage. Fig. 9 presented the stiffness model of the XYZ θ stage excluding one limb. In order to obtain the input stiffness and amplification ratio, the force analysis is obligato. According to the force analysis results, the algebraic expressions of input stiffness and amplification ratio are derived by using the principle of virtual work.

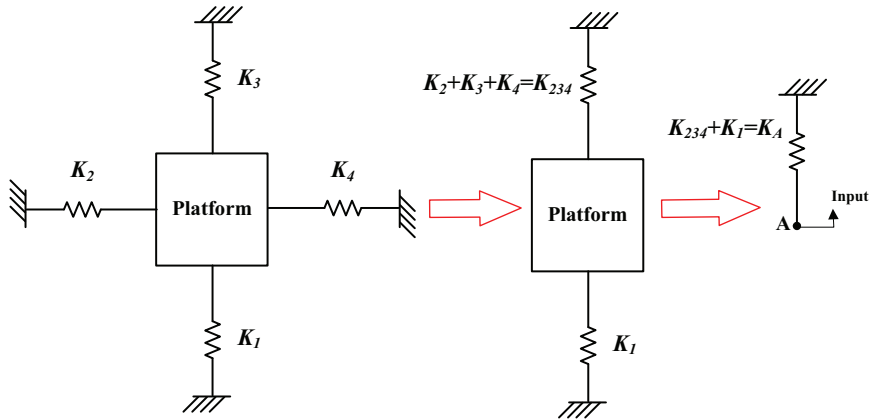


Figure 9: The stiffness model of the XYZ θ stage excluding one limb.

3.1.1. Force analysis of the dual-stage amplifier and Z-shape motion steering mechanism

A. Force analysis of first-stage amplifier

Fig. 10 shows a half of one limb of the XYZ θ stage. Fig. 11 presents the force and moment of force analysis at the static state. M_{r1} and M_{r2} are the internal torque of the flexure hinges when the flexure hinges occur rotation. According to static force and static moment analysis method, the equations can be derived as follows:

$$F_{B1x} = F_{C1x} = F_{D1x} = F_{E1x} = \frac{1}{2}F_{in} = F_x \quad (3)$$

$$F_{B1y} = F_{C1y} = F_{D1y} = F_{E1y} = F_y \quad (4)$$

For the member bar B_1C_1 ,

$$F_{B1x}L_5 = F_{B1y}L_2 + 2M_{r1} \quad (5)$$

$$M_{r1} = K_r\Delta\alpha \quad (6)$$

$$L_2 = L \cos \alpha \quad (7)$$

$$L_5 = L \sin \alpha, \quad (8)$$

where $\Delta\alpha$ is the rotation angle of the flexure hinge around central axis.

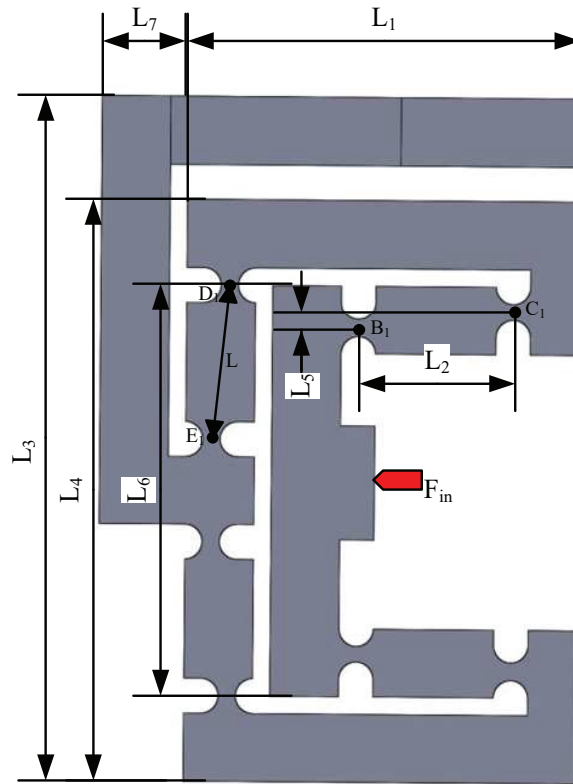


Figure 10: A half of one limb of the XYZ stage.

Substituting Eq.(6) into Eq.(5) and combined with Eq.(7)(8), yields the following:

$$F_{B1x}L \sin \alpha - F_{B1y}L \cos \alpha = 2K_r\Delta\alpha. \quad (9)$$

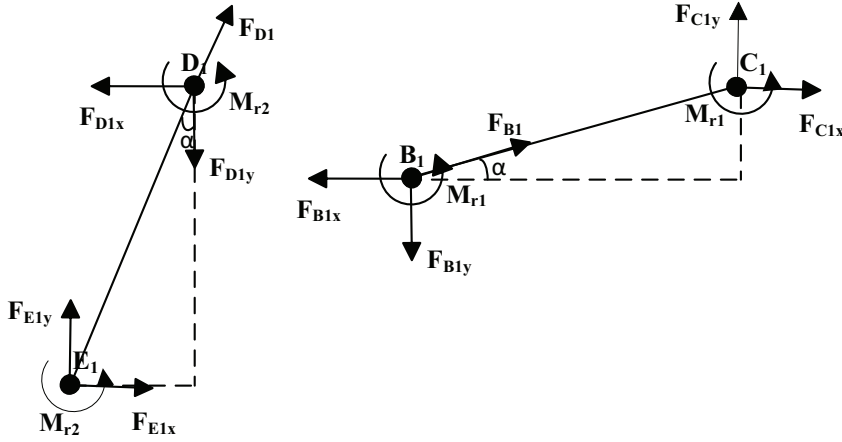


Figure 11: The force and moment of force analysis at the static state.

Also, according to the principle of virtual work, it can be derived that

$$F_{B1x}\Delta x_1 - F_{B1y}\Delta y_1 = F_{B1}\Delta L + 2M_{r1}\Delta\alpha, \quad (10)$$

where F_{B1} is the internal force in the flexure hinge leg B_1C_1 . Δx_1 and Δy_1 are the input and output displacements of the flexure hinge leg B_1C_1 for the first-stage bridge amplifier. And it can be obtained from Fig.10 that

$$F_{B1} = F_{B1x} / \cos \alpha = K_t \Delta L. \quad (11)$$

On the other hand, according to the trigonometric functions, it can be deduced that

$$\begin{aligned} \Delta y_1 &= L \sin(\alpha + \Delta\alpha) - L \sin \alpha \\ &= L \sin \alpha \cos \Delta\alpha + L \cos \alpha \sin \Delta\alpha - L \sin \alpha \\ &\approx L \cos \alpha \Delta\alpha. \end{aligned} \quad (12)$$

B. Force analysis of second-stage amplifier

In consideration of the free body of the flexure hinge leg D_1E_1 and the relationship between the D_1E_1 and B_1C_1 , the following equations are easily obtained:

$$F_{D1y}L_5 = F_{D1x}L_2 + 2M_{r2} \quad (13)$$

$$M_{r2} = K_r \Delta\beta \quad (14)$$

$$F_{D1} = F_{D1y} / \cos \alpha = K_t \Delta L, \quad (15)$$

where M_{r2} is the internal torque of the flexure hinge D_1 and E_1 when the flexure hinge occurring rotation angle $\Delta\beta$ around the center axis. Similar with the analysis method of the first-stage amplifier, denoting Δy_2 and Δx_2 are the input and output stroke, it can be derived

$$F_{D1y}\Delta y_2 - F_{D1x}\Delta x_2 = F_{D1}\Delta L + 2M_{r2}\Delta\beta. \quad (16)$$

Due to $\Delta y_2 = \Delta y_1$, hence

$$F_{D1y}\Delta y_1 - F_{D1x}\Delta x_2 = F_{D1}\Delta L + 2M_{r2}\Delta\beta. \quad (17)$$

In addition, according to Eq.(12), it can be deduced that

$$\Delta x_2 \approx L \cos \alpha \Delta \beta. \quad (18)$$

C. Force analysis of the Z-shape mechanism

The parameters and force analysis of a half Z-shape mechanism is shown in Fig. 12. In view of the force analysis at the balance state, it can be obtained that

$$F_{Gx} = F_{Hx} = F_{E1x} = F_x \quad (19)$$

$$F_{Gz} = F_{Hz} = F_z. \quad (20)$$

For the free body of member bar GH described in Fig.11,

$$F_{Gx}L_{10} = 2M_{r3} \quad (21)$$

$$M_{r3} = K_r \Delta \gamma, \quad (22)$$

where M_{r3} is the internal torque of the flexure hinge G and H when the flexure hinge occurring rotation angle $\Delta \gamma$ around the center axis.

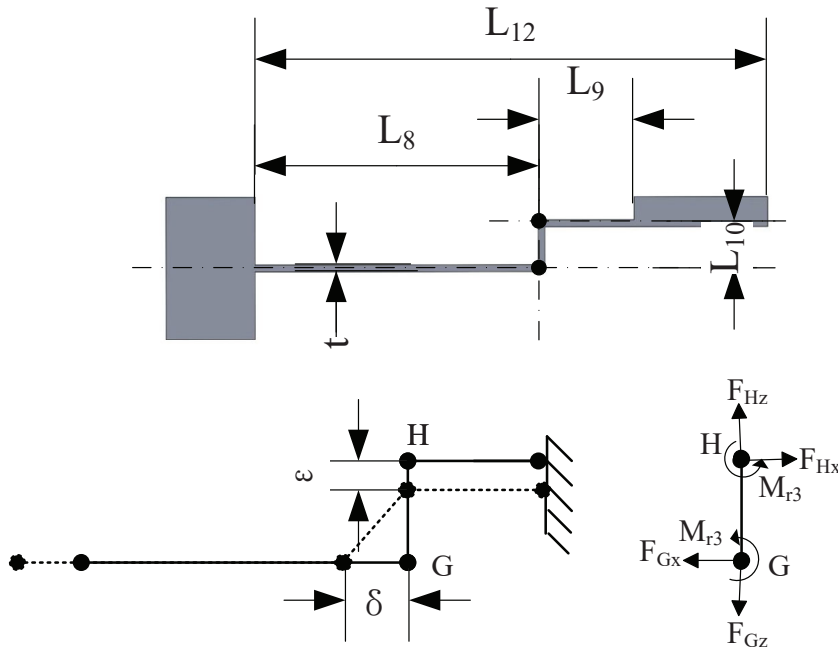


Figure 12: The parameters and force analysis of a half Z-shape mechanism.

As described in Fig. 12, the following equation can be derived for the free body GH :

$$F_x \delta = 2M_{r3} \Delta \gamma \quad (23)$$

$$\epsilon = L_{10} - \sqrt{L_{10}^2 - \delta^2}. \quad (24)$$

In addition, the potential energy stored in Z-shape mechanism can be expressed as

$$P_{GH} = P_1 = \frac{1}{2} K_1 \delta^2 = 2 \times 0.5 K_r \Delta \gamma^2. \quad (25)$$

In consideration of $\Delta \gamma = \frac{\delta}{L_{10}}$, the stiffness of Z-shape mechanism can be derived that

$$K_1 = \frac{2K_r}{L_{10}^2}. \quad (26)$$

3.1.2. The output stiffness analysis of the platform

As shown in Fig. 9, the output stiffness of the platform is relevant to the four limbs. Assuming the output displacement of the stage is ε . Then, it can be deduced that

$$F_{Gx} = K_A \delta, \quad (27)$$

where K_A is the one-dimensional output stiffness of the stage for the input position A.

The other three limbs will produce parasitical motion while the platform is driven by one of the amplifiers. Assuming the output displacement of the platform is d_{out} . The following equations can be derived using potential energy method:

$$P_2 = 4 \times 0.5 K_r \theta^2 = 0.5 K_2 d_{out}^2, \quad (28)$$

where $\theta = d_{out}/L_{11}$ is the rotation angle of flexure hinges in decoupled mechanism. Substituting θ into Eq.(28), it can be calculated that

$$K_2 = \frac{4K_r}{L_{11}^2}. \quad (29)$$

In view of the symmetry of the structure, we can learn that $K_2 = K_4$. In addition, K_3 can be derived from the principle of vertical force at the free end of a cantilever beam [32],

$$K_3 = 2.258 \frac{EI}{L_{12}}, \quad (30)$$

where E is Youngs modulus for the beam material, I is the second moment of area of the cross section.

Considering the parallel connection of K_2, K_3, K_4 , hence

$$\begin{aligned} K_{234} &= K_2 + K_3 + K_4 \\ &= \frac{8K_r}{L_{11}^2} + 2.258 \frac{EI}{L_{12}}. \end{aligned} \quad (31)$$

Combined with the input stiffness of Z-shape mechanism Eq.(26), in consideration of the serial connection of K_1 and K_{234} , the stiffness of point A can be deduced as

$$K_A = \frac{K_1 K_{234}}{K_1 + K_{234}} = \frac{2K_r \left(\frac{8K_r}{L_{11}^2} + 2.258 \frac{EI}{L_{12}} \right)}{L_{10}^2 \left(\frac{2K_r}{L_{10}^2} + \frac{8K_r}{L_{11}^2} + 2.258 \frac{EI}{L_{12}} \right)}. \quad (32)$$

3.1.3. Input stiffness of one limb and amplification ratio of the whole stage

The aims of the kinematics and statics analysis are to derive the input stiffness K_{in} and the ratio of input and output displacement in terms of F_{in} only. In order to calculate the input stiffness K_{in} , the input displacement Δx_1 in terms of F_{in} should be deduced.

The first step is to derive the input stiffness at the point D_1 . In view of Eq.(13)(14)(18)(27) and $\frac{1}{2} F_{Gx} = F_{D1x}$, $\Delta x_2 = \delta$, it can be obtained that

$$\Delta \beta = \frac{F_{D1y} L_5}{0.5 L_2 K_A L \cos \alpha + 2 K_r} \quad (33)$$

$$\Delta x_2 = \frac{F_{D1y} L_5 L \cos \alpha}{0.5 L_2 K_A L \cos \alpha + 2 K_r}. \quad (34)$$

Substituting Eq.(14)(15)(33)(34) into Eq.(16), it can be calculated that

$$\Delta y_2 = F_{D1y} \left[\frac{0.5 K_A \left(\frac{L_5 L \cos \alpha}{0.5 L_2 K_A L \cos \alpha + 2 K_r} \right)^2 + \frac{1}{\cos^2 \alpha K_t}}{+ 2 K_r \left(\frac{L_5}{0.5 L_2 K_A L \cos \alpha + 2 K_r} \right)^2} \right]. \quad (35)$$

Hence, combined with Eq.(7)(8), the input stiffness at the point D_1 can be deduced as

$$\begin{aligned} K_{D1} &= \frac{F_{D1y}}{\Delta y_2} \\ &= \frac{1}{0.5 K_A \left(\frac{L_5 L \cos \alpha}{0.5 L_2 K_A L \cos \alpha + 2 K_r} \right)^2 + \frac{1}{\cos^2 \alpha K_t} + 2 K_r \left(\frac{L_5}{0.5 L_2 K_A L \cos \alpha + 2 K_r} \right)^2} \\ &= \frac{1}{0.5 K_A \left(\frac{L^2 \sin \alpha \cos \alpha}{0.5 K_A L^2 \cos^2 \alpha + 2 K_r} \right)^2 + \frac{1}{\cos^2 \alpha K_t} + 2 K_r \left(\frac{L \sin \alpha}{0.5 K_A L^2 \cos^2 \alpha + 2 K_r} \right)^2} \end{aligned} \quad (36)$$

The second step is to calculate the input stiffness of the whole stage. As shown in Fig. 11. The following equation can be derived

$$F_{D1y} = F_{B1y} = K_{D1} \Delta y_2 \quad (37)$$

$$\Delta y_1 = \Delta y_2. \quad (38)$$

In view of Eq.(9)(12)(37)(38), the value of $\Delta \alpha$ can be derived as

$$\Delta \alpha = \frac{F_{B1x} L \sin \alpha}{L^2 \cos^2 \alpha K_{D1} + 2 K_r} \quad (39)$$

Also, in consideration of Eq.(12)(39), the output displacement of first-stage amplifier can be written as

$$\Delta y_1 = \frac{F_{B1x} L^2 \sin \alpha \cos \alpha}{L^2 \cos^2 \alpha K_{D1} + 2 K_r} \quad (40)$$

Substituting Eq.(6)(11)(37)(38)(39)(40) into Eq.(10) can produce

$$\Delta x_1 = \frac{F_{B1x}}{\cos^2 \alpha K_t} + \frac{F_{B1x} L^2 \sin^2 \alpha}{L^2 \cos^2 \alpha K_{D1} + 2 K_r}. \quad (41)$$

Therefore, the input stiffness of the whole stage can be calculated as

$$K_{in} = \frac{F_{B1x}}{\Delta x_1} = \frac{\cos^2 \alpha K_t (L^2 \cos^2 \alpha K_{D1} + 2 K_r)}{L^2 \cos^2 \alpha K_{D1} + 2 K_r + L^2 \sin^2 \alpha \cos^2 \alpha K_t}. \quad (42)$$

Then, the amplification ratio of the dual-stage amplifier can be deduced from Eq.(7)(8)(34)(42) as

$$\begin{aligned} A_a &= \frac{\delta}{\Delta x_1} = \frac{F_{D1y} L_5 L \cos \alpha}{0.5 L_2 K_A L \cos \alpha + 2 K_r} \times \frac{K_{in}}{F_{B1x}} \\ &= \frac{L^2 \sin^2 \alpha \cos^2 \alpha K_t (L^2 \cos^2 \alpha K_{D1} + 2 K_r)}{(0.5 K_A L^2 \cos^2 \alpha + 2 K_r) (L^2 \cos^2 \alpha K_{D1} + 2 K_r + L^2 \sin^2 \alpha \cos^2 \alpha K_t)} \end{aligned} \quad (43)$$

Moreover, as shown in Fig. 9, the following equation can be derived as

$$F_{E1x} = K_A \delta = K_{234} \epsilon \quad (44)$$

Therefore, the amplification of the whole stage for one limb can be obtained from

$$A = \frac{\epsilon}{\Delta x_1} = \frac{K_A \delta / K_{234}}{\Delta x_1} = \frac{\delta K_A}{\Delta x_1 K_{234}} = A_a \frac{K_A}{K_{234}} \quad (45)$$

$$= \frac{2K_r L^2 \sin^2 \alpha \cos^2 \alpha K_l (L^2 \cos^2 \alpha K_{D1} + 2K_r)}{\left[L_{10}^2 \left(\frac{2K_r}{L_{10}^2} + \frac{8K_r}{L_{11}^2} + 2.258 \frac{EI}{L_{12}} \right) (0.5 K_A L^2 \cos^2 \alpha + 2K_r) \right] \times (L^2 \cos^2 \alpha K_{D1} + 2K_r + L^2 \sin^2 \alpha \cos^2 \alpha K_l)}$$

where K_A and K_{D1} have been obtained using the known variables on above sections.

3.2. The reachable workspace analysis

3.2.1. The maximum stroke in X and Y axes

The flexure hinges have the rotation stress σ_r and vertical axial stress σ_t . In this paper, the flexure hinges adopted in this stage mainly suffered the bending moment around rotation axes. Hence, the maximum rotation angle ω_{\max} determined by the maximum rotation stress σ_r^{\max} of the flexure hinges is equivalent to the maximum output displacement. As learned from literature [33], the maximum rotation angle ω_{\max} can be derived from the maximum rotation stress σ_r^{\max} as follows:

$$\omega_{\max} = \frac{\eta^2 f(\eta)}{E(1+\eta)^{9/20} \sigma_r^{\max}}, \quad (46)$$

where σ_r^{\max} is related to σ_y , which is the yield strength of the flexure hinges material. The σ_r^{\max} can be obtained by

$$\sigma_r^{\max} \leq \frac{\sigma_y}{\lambda}, \quad (47)$$

where $\lambda > 1$ is the safety factor.

$$\eta = \frac{t}{2r} \quad (48)$$

is the dimensionless geometry factor.

$$f(\eta) = \frac{1}{2\eta + \eta^2} \left[\frac{3+4\eta+\eta^2}{(1+\eta)(2\eta+\eta^2)} + \frac{6(1+\eta)}{(2\eta+\eta^2)^{1.5}} \tan^{-1} \left(\frac{2+\eta}{\eta} \right)^{0.5} \right] \quad (49)$$

is the dimensionless compliance factor.

The maximum rotation angles ω_{\max} can be occurred in the secondary amplification mechanism and the decoupled mechanism. The maximum XY output displacement determined by rotation angles ω_{\max}^{DE} occurred in the secondary amplification mechanism can be derived as

$$d_{out1}^{\max} = 2 \frac{A}{A_a} L \cos \alpha \omega_{\max}^{DE}. \quad (50)$$

The maximum XY output displacement determined by rotation angles $\omega_{\max}^{Decouple}$ occurred in the decoupled mechanism can be derived as

$$d_{out2}^{\max} = 2L_{11} \omega_{\max}^{Decouple}. \quad (51)$$

The theoretical maximum output displacement can be obtained from

$$d_{XY}^{\max} = \min \{ d_{out1}^{\max}, d_{out2}^{\max} \}. \quad (52)$$

3.2.2. The maximum stroke in Z axis

The output displacement in Z axis is related to the first-stage amplifier. It can be derived as

$$d_Z^{\max} = 2L \cos \alpha \omega_{\max}^{BC}. \quad (53)$$

3.2.3. The maximum platform rotation angle θ^{\max}

The maximum platform rotation angle θ^{\max} will be occurred when the one limb reaches the maximum stroke in Z axis. Therefore, the maximum platform rotation angle θ^{\max} can be derived as

$$\theta^{\max} = \arctan \frac{2d_Z^{\max}}{L_{13}} = \arctan \frac{4L \cos \alpha \omega_{\max}^{BC}}{L_{13}}. \quad (54)$$

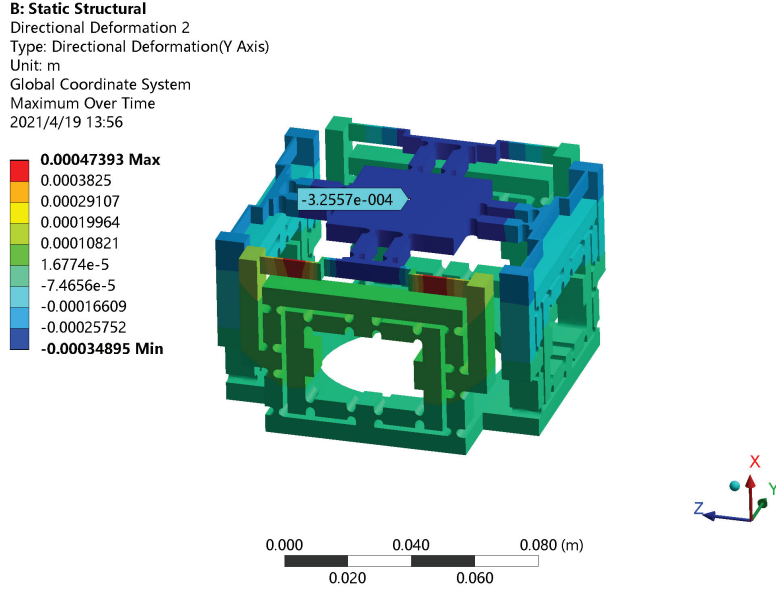


Figure 13: The maximum output displacement in horizontal direction.

Table 1

The parameters of the structure

Dual-stage bridge amplifier structure		Z-shape mechanism structure	
Symbol	Value(mm)	Symbol	Value(mm)
r	1.5	t	1
t	1.5	L_8	19
h	6	L_9	6.5
w	9.5	L_{10}	3.45
L	13.58	L_{12}	34.5
L_1	33	Decoupling mechanism structure	
L_2	13.5	Symbol	Value(mm)
L_3	60	L_{11}	17.2
L_4	51	L_{13}	88
L_5	1.5		
L_6	36		
L_7	7.5		

4. Model validation with simulation

The parameters of the structure and the material properties are illustrated in Table 1 and Table 2. In this section, the model of the stage was analyzed using the finite element analysis software. The material of the stage adopts

B: Static Structural

Directional Deformation
 Type: Directional Deformation(X Axis)
 Unit: m
 Global Coordinate System
 Maximum Over Time
 2021/4/19 14:50

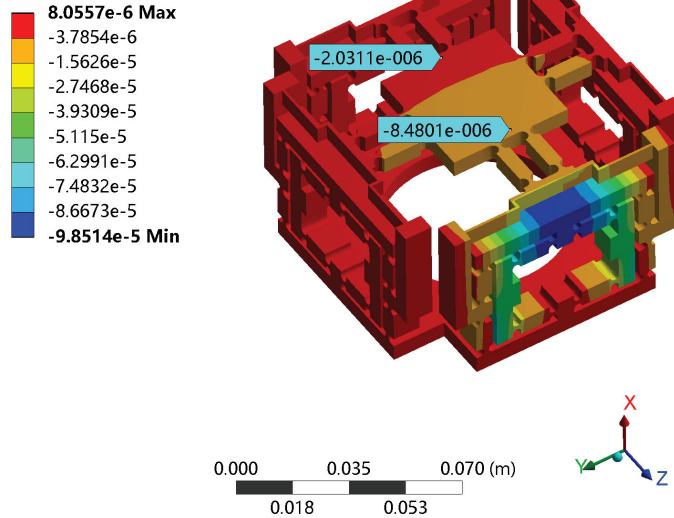


Figure 14: The maximum rotation angle θ around Y axis.

Table 2

The material properties of photopolymer

Parameter	Value	Unit
Poisson's ratio	0.41	-
Young's modulus	2650	MPa
Yield strength	67	MPa
Density	1210	kg/m^3

Table 3

The comparison between mathematical calculation and FEA simulation

	Mathematical calculation	FEA
Horizontal output displacement	0.3173 mm	0.3256 mm
Vertical output displacement	0.0511 mm	0.0402 mm
Rotation angle	$1.02 \times 10^{-4} rad$	$1.535 \times 10^{-4} rad$
Input stiffness	337.21 N/mm	322.99 N/mm
Amplification ratio	14.57	16.28

photopolymer which is beneficial to establish prototype using 3D printing technology. The simulations can verify the output displacement amplification ratio, the input stiffness of the stage, the maximum output displacements, and the maximum output rotation angles. Otherwise, the natural frequencies of the whole stage were obtained with the finite element analysis method which can lay the foundations for the experiments. Fig. 13 shows the maximum output displacement in horizontal direction. The PEA 1 is as the actuator while the other three PEAs do not work. The input displacement and output displacement are 0.02 mm and 0.3256 mm, respectively. Fig. 14 shows the maximum rotation angle θ around Y axis. According to simulation, the maximum rotation angle θ is $1.535 \times 10^{-4} rad$. Fig. 15 shows

B: Static Structural

Directional Deformation
Type: Directional Deformation(X Axis)
Unit: m
Global Coordinate System
Maximum Over Time
2021/4/19 15:44

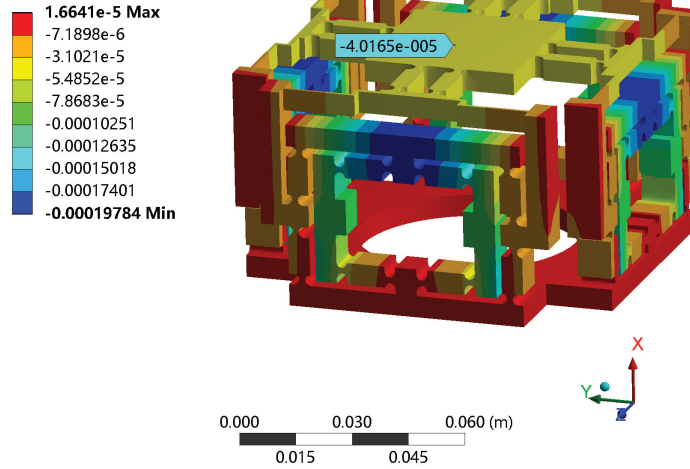
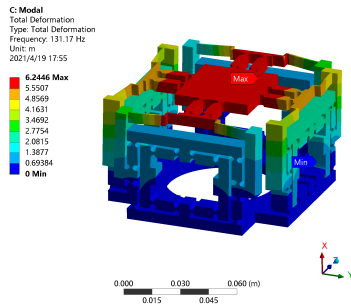
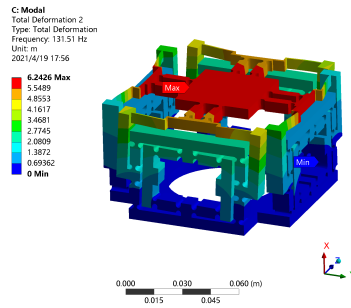


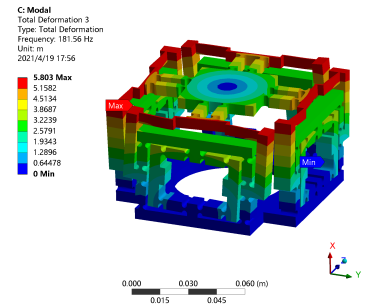
Figure 15: The maximum output displacement in vertical direction.



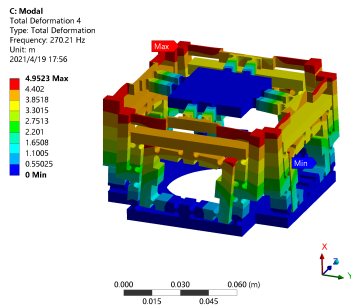
(a) First natural frequency 131.17Hz.



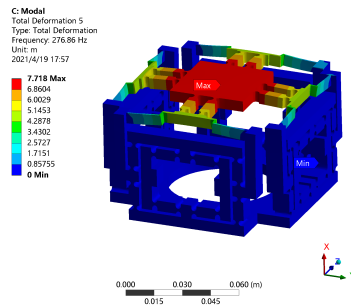
(b) Second natural frequency 131.51Hz.



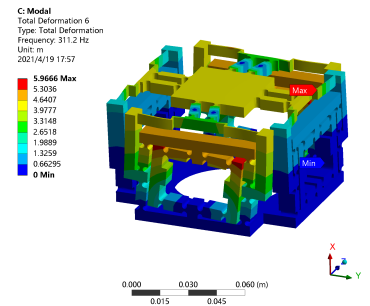
(c) Third natural frequency 181.56Hz.



(d) Fourth natural frequency 270.21Hz.



(e) Fifth natural frequency 276.86Hz.



(f) Sixth natural frequency 311.2Hz.

Figure 16: The natural frequencies of different model shapes.

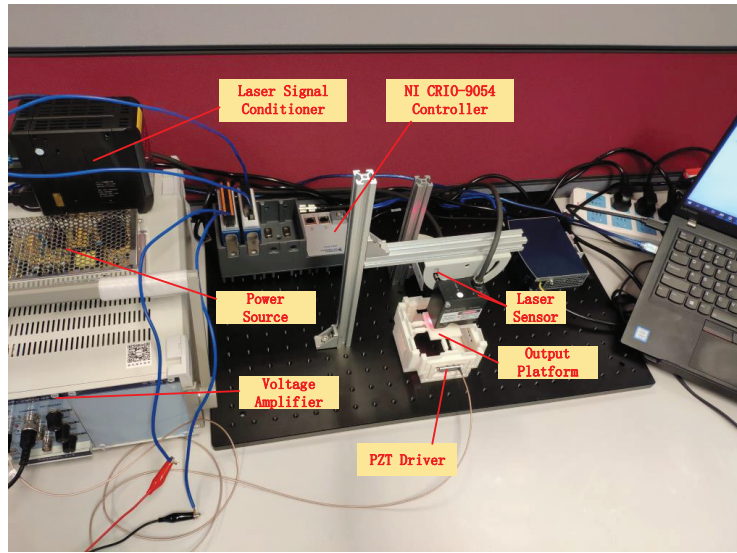


Figure 17: The experimental setup and prototype of the $XYZ\theta$ stage.

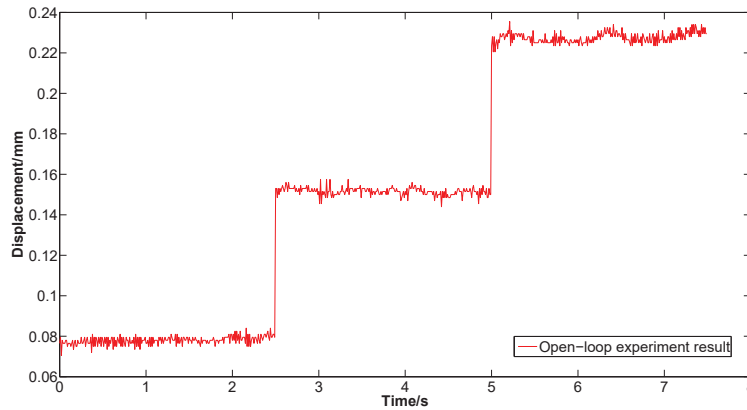


Figure 18: The open-loop control horizontal output displacement.

the maximum output displacement in vertical direction. The four PEAs produce 0.02 mm input displacement that can lead to 0.0402 mm output displacement of the vertical direction. The comparison between mathematical calculation and FEA simulation is shown in Table 3.

The last step is to simulate the natural frequencies of different model shapes as shown in Fig. 16.

5. Prototype fabrication and Experimental studies

In this section, a prototype of the designed compact decoupled $XYZ\theta$ stage was established by 3D printing method with photopolymer material. The experimental platform consists of the control module, the driver module and the measuring module. The setup of experiment is shown in Fig. 17. The stage is driven by four piezoelectric actuators. The output displacements including vertical direction and horizontal direction as well as the rotation angle can be detected by laser displacement sensor. The resolution of the laser sensor is 50nm. The control module includes the host PC, NI CompactRIO-9054 and C series I/O module NI 9201 and NI 9264. The test items including the open loop control output performance analysis and the closed loop control output performance analysis. The output motions directions are divided into vertical direction, horizontal direction and rotational direction due to the symmetry of the $XYZ\theta$ stage.

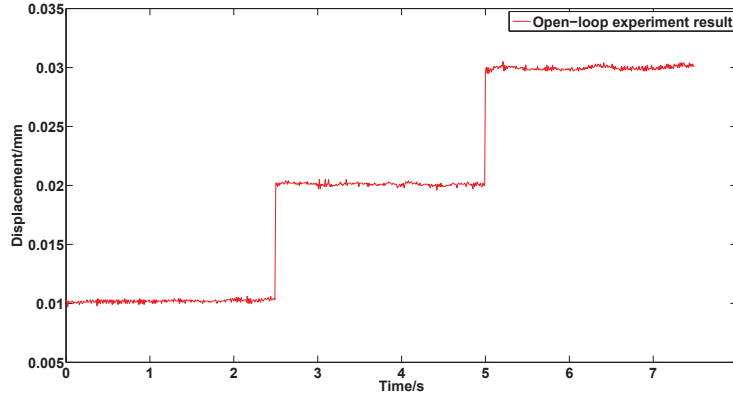


Figure 19: The open-loop control vertical output displacement.

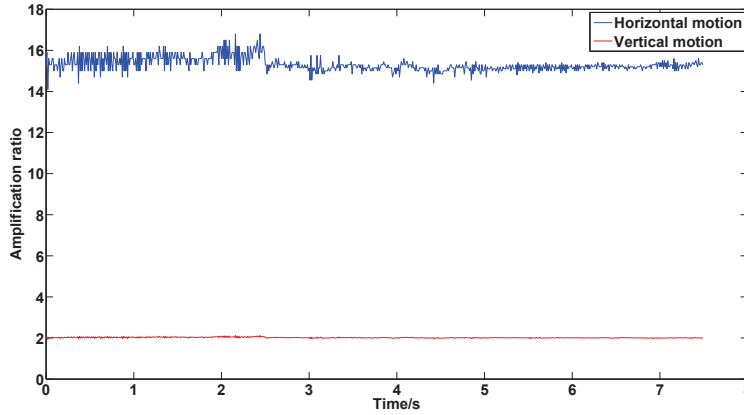


Figure 20: The practical amplification ratio of the stage in horizontal direction and vertical direction.

5.1. The open-loop control output motion analysis

The first step is to test the amplification ratio of the stage. A set of input displacements 5μm, 10μm and 15μm are applied to the driver PZT. Respectively, the output displacements in horizontal direction and vertical direction as shown in Fig. 18 and Fig. 19. The practical amplification ratio results are shown in Fig. 20. Fig. 20 indicates the practical amplification ratio of horizontal output is 15.5 and the practical amplification ratio of vertical output is 2. In Fig. 21, it shows the open-loop output rotation angle.

5.2. The closed-loop control output motion analysis

The objective of the closed-loop control test is to validate the performance of the designed micromotion XYZθ stage. In this section, the control method adopted for PID control and the sample frequency is set to 0.01s. The feedback signal of the output displacement is captured by laser displacement sensor (KEYENCE, LK-H025).

The stairstep signal, square signal and sinusoidal signal trajectory tracking tests are respectively conducted in horizontal output, vertical output, and rotational output. As shown in Fig. 22, a stairstep output trajectory is tracked with high precision. The error recorded in Fig. 22 shows that the maximum peak to peak error is 4.4μm. Then, the square signal trajectory tracking test applied to vertical output performance evaluation. The trajectory tracking experiment result is shown in Fig. 23. The maximum peak to peak error is 1μm as shown in Fig. 23. Finally, the sinusoidal signal trajectory tracking test is implemented in the rotational direction. The test result and the tracking error is presented in Fig. 24. The maximum peak to peak error is 1.67×10^{-5} rad.

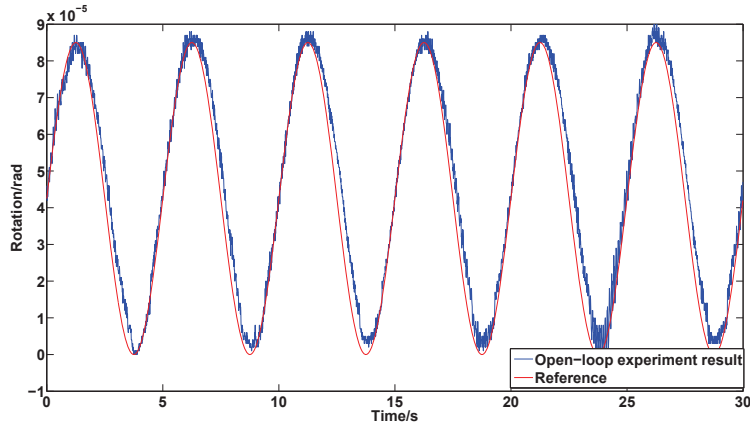
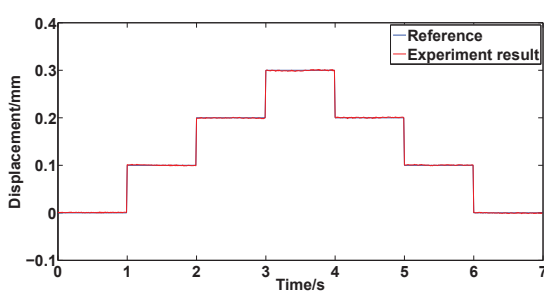
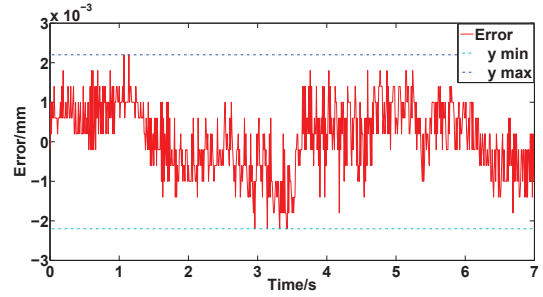


Figure 21: The open-loop control rotational output angle.

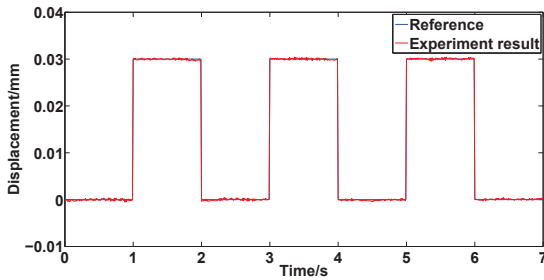


(a) The closed-loop control horizontal output displacement.

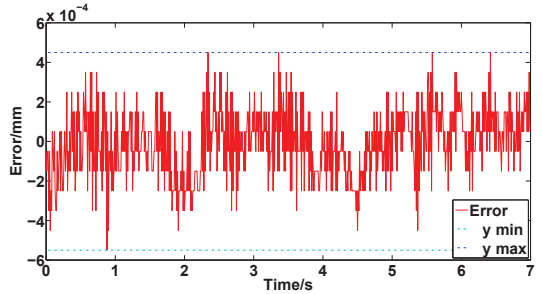


(b) The error of closed-loop control horizontal output displacement.

Figure 22: The closed-loop output displacement in horizontal direction.



(a) The closed-loop control vertical output displacement.

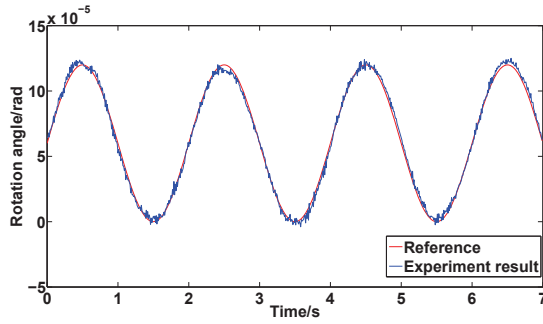


(b) The error of closed-loop control vertical output displacement.

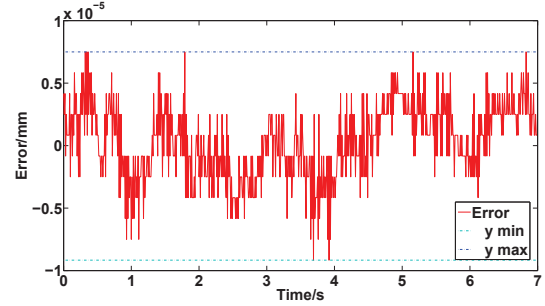
Figure 23: The closed-loop output displacement in vertical direction.

6. Conclusion

In this paper, a new XYZ θ ultra compact decoupled high precision motion stage (UCDS) is designed and analyzed. The XYZ θ UCDS contains four limbs and every limb consists of a dual-stage bridge amplifier and a Z-shape mechanism which can change the direction of motion transfer. Then, the kinetostatic analysis of this new XYZ θ stage is conducted including the input stiffness of the stage, the maximum output displacements and rotation angles in different direction and axis. The simulation utilizing finite element method is implemented to verify the theoretical analysis results. The simulation of the UCDS shows that the maximum horizontal output displacement is 0.3256 mm, the



(a) The closed-loop control rotational output angle.



(b) The error of closed-loop control rotational output angle.

Figure 24: The closed-loop output angle in rotational direction.

maximum vertical output displacement is 0.0402 mm and the maximum rotation angle is 1.535×10^{-4} rad. Finally, a prototype is built and a series of experiments in terms of open-loop control test and closed-loop control test are implemented. The practical amplification ratio are 15.5 in XY directions and 2 in Z direction. The closed-loop control positioning accuracy are 4.4 μ m in XY directions, 1 μ m in Z direction and 1.67×10^{-5} rad.

Declaration of Competing Interest

No conflict of interest exists in the submission of this manuscript, and manuscript is approved by all authors for publication. I would like to declare on behalf of my coauthors that the work described was original research that has not been published previously, and not under consideration for publication elsewhere, in whole or in part. All the authors listed have approved the manuscript that is enclosed.

Acknowledgement

The authors would like to thank the support provided by the National Natural Science Foundation of China (Grant No. 51575544), the General Research Fund (GRF) of the Research Grants Council (RGC) of Hong Kong, China (Grant No. PolyU 152137/19E), and the Research Committee of Hong Kong Polytechnic University (Grant No.1-45-37-ZE97).

References

- [1] Y. Li, Q. Xu, A novel design and analysis of a 2-dof compliant parallel micromanipulator for nanomanipulation, *IEEE Trans. Autom. Sci. Eng.* 3 (2006) 247–254. doi:10.1109/TASE.2006.875533.
- [2] G. Hao, X. He, S. Awtar, Design and analytical model of a compact flexure mechanism for translational motion, *Mech. Mach. Theory* 142 (2019) 103593. URL: <https://www.sciencedirect.com/science/article/pii/S0094114X19309711>. doi:https://doi.org/10.1016/j.mechmachtheory.2019.103593.
- [3] Y. Li, Q. Xu, Modeling and performance evaluation of a flexure-based xy parallel micromanipulator, *Mech. Mach. Theory* 44 (2009) 2127–2152. URL: <https://www.sciencedirect.com/science/article/pii/S0094114X09001141>. doi:https://doi.org/10.1016/j.mechmachtheory.2009.06.002.
- [4] A. Al-Jodah, B. Shirinzadeh, M. Ghafarian, T. K. Das, J. Pinskiar, Design, modeling, and control of a large range 3-dof micropositioning stage, *Mech. Mach. Theory* 156 (2021) 104159. URL: <https://www.sciencedirect.com/science/article/pii/S0094114X20303761>. doi:https://doi.org/10.1016/j.mechmachtheory.2020.104159.
- [5] A. Al-Jodah, B. Shirinzadeh, M. Ghafarian, T. K. Das, J. Pinskiar, Y. Tian, D. Zhang, Modeling and a cross-coupling compensation control methodology of a large range 3-dof micropositioner with low parasitic motions, *Mech. Mach. Theory* 162 (2021) 104334. URL: <https://www.sciencedirect.com/science/article/pii/S0094114X21000926>. doi:https://doi.org/10.1016/j.mechmachtheory.2021.104334.
- [6] L. L. Howell, *Compliant mechanisms*, in: 21st century kinematics, Springer, 2013, pp. 189–216.
- [7] R. Li, Z. Yang, G. Chen, B. Wu, Analytical solutions for nonlinear deflections of corner-fillet leaf-springs, *Mech. Mach. Theory* 157 (2021) 104182. URL: <https://www.sciencedirect.com/science/article/pii/S0094114X20303992>. doi:https://doi.org/10.1016/j.mechmachtheory.2020.104182.
- [8] P. P. Valentini, M. Cirelli, E. Pennestrì, Second-order approximation pseudo-rigid model of flexure hinge with parabolic variable thickness,

- Mech. Mach. Theory 136 (2019) 178–189. URL: <https://www.sciencedirect.com/science/article/pii/S0094114X19300680>. doi:<https://doi.org/10.1016/j.mechmachtheory.2019.03.006>.
- [9] K. Wu, G. Zheng, G. Hao, Efficient spatial compliance analysis of general initially curved beams for mechanism synthesis and optimization, Mech. Mach. Theory 162 (2021) 104343. URL: <https://www.sciencedirect.com/science/article/pii/S0094114X21001014>. doi:<https://doi.org/10.1016/j.mechmachtheory.2021.104343>.
 - [10] H. Tang, J. Gao, X. Chen, K. Yu, S. To, Y. He, X. Chen, Z. Zeng, S. He, C. Chen, Y. Li, Development and repetitive-compensated pid control of a nanopositioning stage with large-stroke and decoupling property, IEEE Trans. Ind. Electron. 65 (2018) 3995–4005. doi:10.1109/TIE.2017.2758749.
 - [11] S. Wu, Z. Shao, H. Su, H. Fu, An energy-based approach for kinetostatic modeling of general compliant mechanisms, Mech. Mach. Theory 142 (2019) 103588. URL: <https://www.sciencedirect.com/science/article/pii/S0094114X19311838>. doi:<https://doi.org/10.1016/j.mechmachtheory.2019.103588>.
 - [12] X. Chen, Y. Li, A new structure to achieve large-scale damage-avoiding capture based on compliant mechanism, Microsyst. Technol. (2020) 1–8. doi:10.1007/s00542-020-04989-1.
 - [13] Y. Xie, Y. Li, C. F. Cheung, Z. Zhu, X. Chen, Design and analysis of a novel compact xyz parallel precision positioning stage, Microsyst. Technol. (2020) 1–8. doi:10.1007/s00542-020-04968-6.
 - [14] F. Wang, X. Zhao, Z. Huo, B. Shi, C. Liang, Y. Tian, D. Zhang, A 2-dof nano-positioning scanner with novel compound decoupling-guiding mechanism, Mech. Mach. Theory 155 (2021) 104066. URL: <https://www.sciencedirect.com/science/article/pii/S0094114X2030286X>. doi:<https://doi.org/10.1016/j.mechmachtheory.2020.104066>.
 - [15] R. Lin, Y. Li, Y. Zhang, T. Wang, Z. Wang, Z. Song, Z. Dou, J. Qian, Design of a flexure-based mixed-kinematic xy high-precision positioning platform with large range, Mech. Mach. Theory 142 (2019) 103609. URL: <https://www.sciencedirect.com/science/article/pii/S0094114X19316647>. doi:<https://doi.org/10.1016/j.mechmachtheory.2019.103609>.
 - [16] S. Li, G. Hao, W. M. Wright, Design and modelling of an anti-buckling compliant universal joint with a compact configuration, Mech. Mach. Theory 156 (2021) 104162. URL: <https://www.sciencedirect.com/science/article/pii/S0094114X20303797>. doi:<https://doi.org/10.1016/j.mechmachtheory.2020.104162>.
 - [17] Y. K. Yong, S. S. Aphale, S. O. R. Moheimani, Design, identification, and control of a flexure-based xy stage for fast nanoscale positioning, IEEE Trans. Nanotechnol. 8 (2009) 46–54. doi:10.1109/TNANO.2008.2005829.
 - [18] P. Gao, S.-M. Swei, Z. Yuan, A new piezodriven precision micropositioning stage utilizing flexure hinges, Nanotechnology 10 (1999) 394–398. URL: <https://doi.org/10.1088/0957-4484/10/4/306>. doi:10.1088/0957-4484/10/4/306.
 - [19] M. L. Culpepper, G. Anderson, Design of a low-cost nano-manipulator which utilizes a monolithic, spatial compliant mechanism, Precis. Eng. 28 (2004) 469–482. URL: <https://www.sciencedirect.com/science/article/pii/S014163590400090X>. doi:<https://doi.org/10.1016/j.precisioneng.2004.02.003>.
 - [20] M. Ling, J. Cao, Z. Jiang, J. Lin, Theoretical modeling of attenuated displacement amplification for multistage compliant mechanism and its application, Sens. Actuators, A 249 (2016) 15–22. URL: <https://www.sciencedirect.com/science/article/pii/S0924424716303867>. doi:<https://doi.org/10.1016/j.sna.2016.08.011>.
 - [21] Y. Li, Q. Xu, Design and analysis of a totally decoupled flexure-based xy parallel micromanipulator, IEEE Trans. Robot. 25 (2009) 645–657. doi:10.1109/TR0.2009.2014130.
 - [22] Y. Jiang, T.-M. Li, L.-P. Wang, Stiffness modeling of compliant parallel mechanisms and applications in the performance analysis of a decoupled parallel compliant stage, Rev. Sci. Instrum. 86 (2015) 095109. doi:10.1063/1.4930884.
 - [23] X. Chen, Y. Li, Design and analysis of a new high precision decoupled xy compact parallel micromanipulator, Micromachines 8 (2017). URL: <https://www.mdpi.com/2072-666X/8/3/82>. doi:10.3390/mi8030082.
 - [24] M. Ling, J. Cao, Q. Li, J. Zhuang, Design, pseudostatic model, and pvdF-based motion sensing of a piezo-actuated xyz flexure manipulator, IEEE/ASME Trans. Mechatronics 23 (2018) 2837–2848. doi:10.1109/TMECH.2018.2871371.
 - [25] Y. Li, Q. Xu, A totally decoupled piezo-driven xyz flexure parallel micropositioning stage for micro/nanomanipulation, IEEE Trans. Autom. Sci. Eng. 8 (2011) 265–279. doi:10.1109/TASE.2010.2077675.
 - [26] N. Lobontiu, Compliant mechanisms: design of flexure hinges, CRC press, 2002.
 - [27] L. Li, D. Zhang, S. Guo, H. Qu, Design, modeling, and analysis of hybrid flexure hinges, Mech. Mach. Theory 131 (2019) 300–316. URL: <https://www.sciencedirect.com/science/article/pii/S0094114X18303562>. doi:<https://doi.org/10.1016/j.mechmachtheory.2018.10.005>.
 - [28] L. Qiu, Y. Liu, Y. Yu, Y. B. Bai, Design and stiffness analysis of a pitch-varying folded flexure hinge (pffh), Mech. Mach. Theory 157 (2021) 104187. URL: <https://www.sciencedirect.com/science/article/pii/S0094114X20304043>. doi:<https://doi.org/10.1016/j.mechmachtheory.2020.104187>.
 - [29] K. Xu, H. Liu, W. Yue, J. Xiao, Y. Ding, G. Wang, Kinematic modeling and optimal design of a partially compliant four-bar linkage using elliptic integral solution, Mech. Mach. Theory 157 (2021) 104214. URL: <https://www.sciencedirect.com/science/article/pii/S0094114X20304316>. doi:<https://doi.org/10.1016/j.mechmachtheory.2020.104214>.
 - [30] Z. Xie, L. Qiu, D. Yang, Analysis of a novel variable stiffness filleted leaf hinge, Mech. Mach. Theory 144 (2020) 103673. URL: <https://www.sciencedirect.com/science/article/pii/S0094114X19322797>. doi:<https://doi.org/10.1016/j.mechmachtheory.2019.103673>.
 - [31] T. Liu, S. Bi, Y. Yao, Z. Dong, Q. Yang, L. Liu, Research on zero-stiffness flexure hinge (zsfh) based on spring four-bar linkage (4bsl), Mech. Mach. Theory 143 (2020) 103633. URL: <https://www.sciencedirect.com/science/article/pii/S0094114X19310493>. doi:<https://doi.org/10.1016/j.mechmachtheory.2019.103633>.
 - [32] L. L. Howell, S. P. Magleby, B. M. Olsen, J. Wiley, Handbook of compliant mechanisms, Wiley Online Library, 2013.
 - [33] S. T. Smith, Flexures: elements of elastic mechanisms, CRC Press, 2000.